Radio Science, Volume 34, Number 6, Pages 1485–1496, November–December 1999

Range imaging using frequency diversity

Robert D. Palmer and Tian-You Yu
Department of Electrical Engineering and Center for Electro-Optics, University of Nebraska, Lincoln

Phillip B. Chilson
MRI Atmospheric Research Programme, Swedish Institute of Space Physics, Kiruna, Sweden

Abstract. The need exists for measurements with high vertical resolution when observing the variety of atmospheric processes with extremely small vertical extent, such as microscale turbulence and scattering layers associated with inertia gravity waves. For example, recent in situ observations have shown that both humidity and temperature "sheets," with thicknesses of the order of meters, exist throughout the lower atmosphere. Hampered by bandwidth constraints, however, standard pulsed radar systems have shown only limited usefulness in the detection of such phenomena. Frequency domain interferometry can be used to estimate the position and thickness of a single scattering layer within the resolution volume. Using two closely spaced frequencies, the method is derived under the restrictive assumption of a single, Gaussian-shaped layer. We will now introduce range imaging (RIM), which fully exploits the general advantages of frequency diversity. Using a set of closely spaced transmitter frequencies, a generalized method based on constrained optimization will be used to reconstruct high-resolution images of the average power density as a function of range. The technique will be studied using simulated radar data and will be shown to be capable of resolving complex structures similar to Kelvin-Helmholtz billows, which can be much smaller in vertical extent than the resolution volume.

1. Introduction

Atmospheric radars are routinely used to study a wide range of dynamic processes that span large-scale motions, such as those found in planetary waves ($\sim 10^7$ m, $\sim 10^6$ s), to small-scale turbulent interactions ($\sim 10^0$ m, $\sim 10^0$ s). In particular, wind profilers such as boundary-layer radars (BLR) and mesosphere-stratosphere-troposphere (MST) radars have proven invaluable to both operational meteorology and research programs. An overview of some current investigations being conducted at various MST facilities and with different techniques is given by *Hocking* [1997].

The atmosphere has shown itself to contain a rich variety of structures in the vertical extent. Whereas these structures can exist with height scales of the order of a meter, bandwidth limitations make it difficult to resolve features this small using conventional pulsed radar technology. Frequency-modulated continuous wave (FMCW) radars are used for high-resolution vertical studies of the atmosphere, and *Eaton et al.* [1995] have described a relatively new state-of-the-art FMCW radar that offers a height resolution of 2 m. In their paper, Eaton et al. demonstrate in particular the applicability of this radar for studies of the planetary boundary layer (PBL). They present remarkable "snapshots" of vertical structures observed by the radar in the lower 3 km of the atmosphere. Some examples of these are Kelvin-Helmholtz (KH) billows created by a low-level jet, a coupling of wave activities with the production of turbulence, and small-scale vertical features associated with a frontal passage.

In situ measurements made from balloon-borne platforms are frequently used to obtain profiles of such atmospheric parameters as wind, humidity, temperature, chemical composition, and so forth. Results of one such experiment revealed the atmosphere

Paper number 1999RS900089.
0048-6604/99/1999RS900089$11.00

up to a height of 27 km to contain a large number of sharp temperature gradients within extremely thin layers of thicknesses less than 10 m [*Dalaudier et al.*, 1994]. These authors (p. 237) maintain that "this unexpected finding has potentially important consequences for the theoretical understanding of small-scale atmospheric dynamical processes and also has practical consequences for all the propagation phenomena (light beams, radio waves, sounds ...) within the atmosphere." In addition to these measurements, *Muschinski and Wode* [1998] have recently identified coexisting atmospheric temperature and humidity sheets with thicknesses down to a few decimeters. Both *Dalaudier et al.* [1994] and *Muschinski and Wode* [1998] discuss the relevance of these sheets to radio frequency scatter/reflection mechanisms.

As discussed by *Hocking* [1987] and *Reid* [1990], layered structures are often observed with radar in the height range of 60-100 km. The layers are in many cases associated with "steps" in the refractive index or localized regions of turbulence. One particular class of radar echo observed within this range are the polar mesosphere summer echoes (PMSE). Although research on PMSE has continued for almost 15 years, the exact scattering mechanism remains unclear [*Cho and Röttger*, 1997]. It is widely accepted, however, that vertical structures such as sharp edges or highly anisotropic scatterers on the edges of turbulent layers could contribute to some PMSE.

As we have tried to illustrate, an investigation of many atmospheric dynamic processes requires measurements having a high vertical resolution. Examples of these are microscale turbulence, wave motions and instabilities having long periods but small amplitudes, and conditions leading to thin layers. If we focus on remote sensing techniques, then we find that FMCW radars provide excellent vertical range resolution but only over a limited height coverage. Pulsed radars are capable of good height coverage, but the range resolution is limited by the pulse width. To overcome this dilemma, a technique has been introduced for which radar measurements are made at two or more closely spaced frequencies [*Kudeki and Stitt*, 1987]. This method, which is called frequency domain interferometry (FDI), makes use of the amplitude and phase of the normalized cross correlation or cross spectrum formed by two frequencies. If a single dominant layer is present within the radar sampling volume, then the amplitude and phase can be used to estimate the width and position, respectively, of the layer.

FDI has found many applications in atmospheric studies. For example, *Chilson et al.* [1997] used FDI in their investigations of an upper level jet stream and were able to observe KH billows in the shear region of the jet. *Muschinski et al.* [1999] have investigated large-scale vertical velocities using the technique. By tracking the position of persisting layers, they estimated vertical velocities with an accuracy of about 1 cm s^{-1}. The resolving power of FDI has also been used in the study of PMSE [*Franke et al.*, 1992]. Recent measurements of PMSE made with the European incoherent scatter (EISCAT) VHF radar in Tromsø, Norway, suggest that FDI might be capable of locating horizontal structures in the plasma within the layers.

There are inherent limitations of any two-frequency FDI analysis. Most important, the original derivation of the FDI analysis assumed a single, Gaussian-shaped scattering layer per sampling volume. However, *Dalaudier et al.* [1994] have shown that sharp gradients can be ubiquitous in the free atmosphere up to 27 km. If several dominating layers are present, then the position and width estimates from the two-frequency FDI analysis provide only the first and second moments of the vertical reflectivity structure within the pulse volume.

The work of *Franke* [1990] provided the theoretical framework for the use of more than two frequencies, where a formula was derived for the average power of a signal obtained from multiple frequencies. The present work serves as an introduction to range imaging (RIM), which is a generalization of the use of frequency diversity where no assumptions are made concerning number of layers and/or layer shape. Further, advanced optimization techniques will be used to enhance the resolution over what can be obtained through standard Fourier analysis. These results will be used to create an estimate of "range brightness," which is the average power density as a function of range. The term brightness is used in order to emphasize the close connection of RIM with coherent radar imaging (CRI), which has recently found favor in estimating the angular dependence of average power [*Kudeki and Sürücü*, 1991; *Hysell*, 1996; *Woodman*, 1997; *Palmer et al.*, 1998]. In CRI, the angular brightness is estimated by using the diversity of signals received by spatially separated antennas on

the ground. RIM uses frequency diversity in order to estimate range brightness. Because of this relationship between CRI and RIM, the derivation of the RIM analysis will be shown to be extremely similar to the CRI case [*Palmer et al.*, 1998].

2. Range Imaging

2.1. Outgrowth of Frequency Domain Interferometry

As stated in the introduction, we would like to expand the idea of FDI to the general case of m different frequencies. The transmitter frequency can be varied from pulse to pulse or possibly transmitted simultaneously if appropriate coherent separation can be achieved. After coherent integration, subject to the same constraints as temporal sampling, the m coherently detected signals will be denoted by $s_1(t)$, $s_2(t)$, ..., $s_m(t)$. By combining these signals into a column vector $\mathbf{s}(t)$, a more compact notation is obtained. The ultimate question is how to use the frequency diversity that exists within the signals spanned by $\mathbf{s}(t)$. Arguably, the simplest composite signal that can be conceived is the weighted summation of the m signals, which is given in matrix notation in the following equation:

$$y(t) = \mathbf{w}^\dagger \mathbf{s}(t), \tag{1}$$

where the dagger represents the Hermitian operator (complex transpose). The complex weights w_1, w_2, ..., w_m, corresponding to each of the coherently detected signals are combined in the column vector $\mathbf{w}$. Note that the weights are complex, thus providing the flexibility of both amplitude and phase modification. Basically, the weight vector will be used to create constructive interference between the m signals at a particular range.

As was mentioned earlier, the derivation of the range brightness estimate is similar to that of CRI used to estimate angular brightness. The main difference is that CRI uses spatial diversity to achieve higher angular resolution, while RIM uses frequency diversity for higher range resolution. A complete derivation for the angular imaging case was provided by *Palmer et al.* [1998].

Assuming wide-sense stationarity of the m signals, the autocorrelation function of $y(t)$ can be shown to have the following form:

$$R_y(\tau) = \mathbf{w}^\dagger \mathbf{R}(\tau) \mathbf{w}, \tag{2}$$

where $\mathbf{R}(\tau)$ is the correlation matrix providing all combinations of the m signals. By taking the Fourier transform of (2), an estimate of the range brightness, based on the linear combination (1), can be obtained,

$$\hat{B}_r(r_I, f) = \mathbf{w}^\dagger \mathbf{V}(f) \mathbf{w}, \tag{3}$$

where r_I is the range to be imaged. The normalized cross-spectral matrix $\mathbf{V}(f)$, which is dependent on temporal frequency f, is given by the following equation and is simply the Fourier transform of $\mathbf{R}(\tau)$:

$$\mathbf{V}(f) = \begin{bmatrix} V_{11}(f) & V_{12}(f) & \cdots & V_{1m}(f) \\ V_{21}(f) & V_{22}(f) & \cdots & V_{2m}(f) \\ \vdots & \vdots & \ddots & \vdots \\ V_{m1}(f) & V_{m2}(f) & \cdots & V_{mm}(f) \end{bmatrix}. \tag{4}$$

The range brightness estimate (3) is based on the linear combination of the signals in $\mathbf{s}(t)$. Different estimates of the range brightness would be obtained if another (possibly nonlinear) use of the frequency diversity were assumed.

The next logical step is to obtain the form of the weighting vector in order to achieve the best range resolution while reducing spurious artifacts. A simple procedure for obtaining $\mathbf{w}$ will be provided in the next section.

2.2. Weight Vector Calculation

In a manner similar to the angular imaging case [*Palmer et al.*, 1998], we will obtain the desired weight vector through the solution of a constrained optimization problem. Such a procedure was first described by *Capon* [1969] for the case of subterranean imaging using a seismic array. The main goal of the optimization will be to minimize the possibility of range sidelobe effects. Therefore we will attempt to minimize the total range brightness with respect to the weighting vector $\mathbf{w}$, which will have the effect of minimizing the contribution to the brightness from ranges other than r_I. The minimization will take place with the constraint that the effective range weighting will be unity at r_I. The problem is stated formally in the following manner:

$$\min_{\mathbf{w}} \hat{B}_r(r_I, f) \text{ subject to } \mathbf{e}_r^\dagger \mathbf{w} = 1, \tag{5}$$

where the "range steering vector" is given by

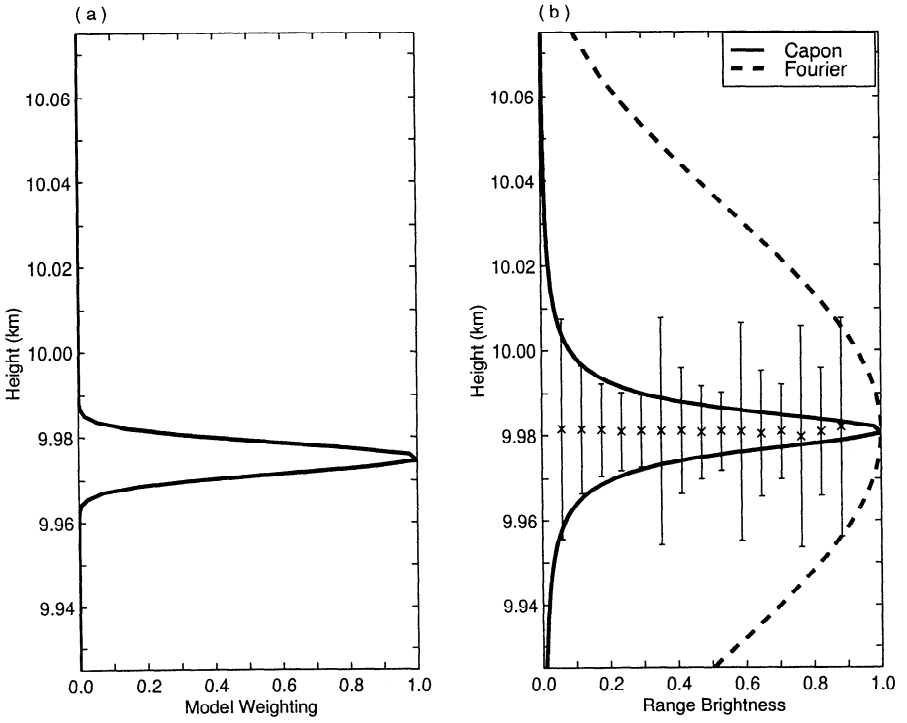

Figure 1. Simulation results (signal-to-noise ratio (SNR)=20 dB) for a single scattering layer within the resolution volume, which is 150 m in vertical extent. The six frequencies used in the simulation are 49.5, 49.7, 49.9, 50.1, 50.3, and 50.5 MHz. Shown are (a) model weighting including the range weighting function, and (b) Capon and Fourier range imaging (RIM) results along with the layer position/width estimates from FDI. Note that with frequency domain interferometry (FDI) using six frequencies, there are 15 frequency pairs available.

$$\mathbf{e}_r = \left[\; e^{-j(2k_1 r_I - \phi_1)} \quad \ldots \quad e^{-j(2k_m r_I - \phi_m)} \; \right]^T. \quad (6)$$

The wavenumbers of the m signals are denoted by k_i for signal i. Note that the elements of $\mathbf{e}_r$ are used to force the m coherently detected signals to constructively interfere at a range of r_I. Therefore the initial phase (ϕ_i) of the m signals must be either known or the same, for all signals. This point will be expanded upon in the next section.

Using Lagrange methods to solve the constrained optimization problem, the optimal weight vector is obtained and can be used for the Capon RIM estimate of range brightness [*Luenberger*, 1984].

$$\hat{B}_{rC}(r_I, f) = \frac{1}{\mathbf{e}_r^\dagger \mathbf{V}^{-1}(f)\mathbf{e}_r} \quad (7)$$

Another more straightforward choice of the weight vector would be to simply use the steering vector $\mathbf{e}_r$ directly in (1). In this case, the Fourier RIM estimate of range brightness is obtained.

$$\hat{B}_{rF}(r_I, f) = \mathbf{e}_r^\dagger \mathbf{V}(f)\mathbf{e}_r \quad (8)$$

It should be noted that the Fourier RIM analysis is similar to that proposed by *Franke* [1990]. As shown by *Palmer et al.* [1998] for the angular imaging case, however, Fourier-based methods inherently have diminished resolution. This characteristic holds true in the RIM case also, which will become evident in the next section.

Basically, the estimation of the range brightness can be thought of as a spectral estimation problem. RIM is simply the spectral estimate of the m signals obtained by varying the transmitter frequency. As such, numerous algorithms exist which may have advantages over Capon's method [*Kay*, 1987]. However, we have observed that Capon's method is extremely

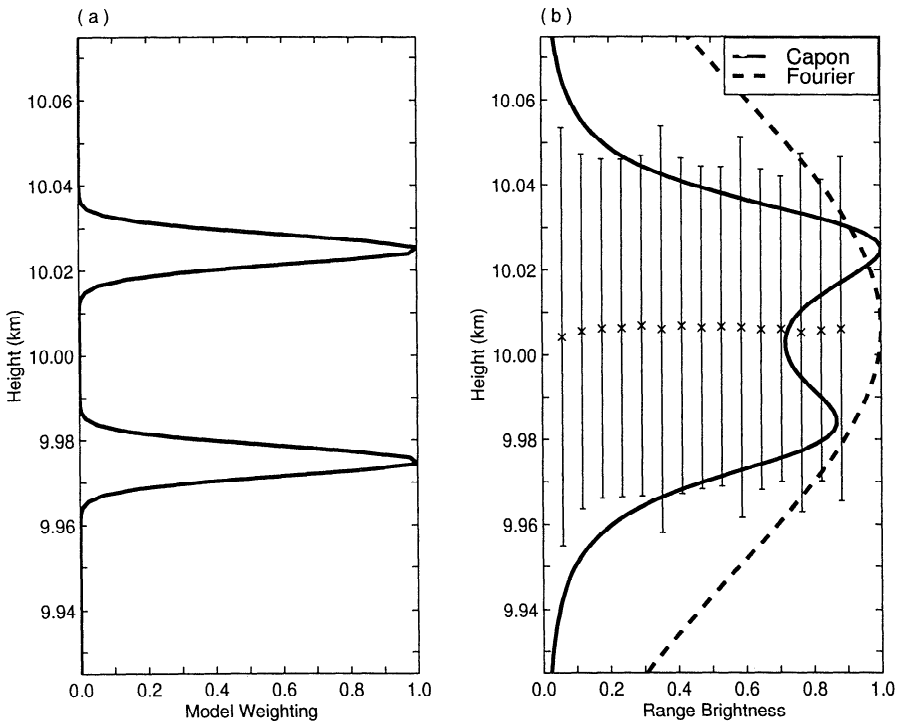

Figure 2. Same as Figure 1, expect for the case of two distinct scattering layers within the resolution volume. Shown are (a) model weighting and (b) Capon and Fourier RIM results along with the layer position/width estimates from FDI. Note that all combinations of FDI results produce similar layer position estimates. In addition, the FDI layer widths are severely biased due to the double layer. Capon RIM is able to resolve the two layers, while Fourier RIM is not.

robust in that spurious artifacts are seldom seen in the range brightness estimates.

3. Simulation Results

As is usually the case with experimental data, the true atmospheric condition is unknown. We have decided to test RIM using simulated data where all atmospheric and experimental conditions are known. An extremely flexible and simple method of simulating atmospheric radar data was developed by *Holdsworth and Reid* [1995]. A three-dimensional field of scattering points is randomly generated and placed within a so-called "enclosing volume." At each time step, the scatterers are allowed to follow a mean flow and a spatially correlated turbulent flow. As scatterers leave the enclosing volume, they are replaced at the opposite three-dimensional position. Thus the enclosing volume is continually filled with scatterers.

As described by *Holdsworth and Reid* [1995], the amplitude of each scattering point is dictated by several parameters, including a random reflectivity, antenna beam pattern, range weighting function, and any aspect sensitivity effects, which are assumed negligible in this case. Aspect sensitivity has a tendency to narrow the effective beam pattern of the radar. Thus we expect that the effect will not be significant for a horizontally stratified atmosphere. Both the antenna beam pattern and the range weighting function have a Gaussian form. The one-way, half-power beam width is 3.6°, and the range weighting function corresponds to a 1-μs pulse, as described by *Doviak and Zrnić* [1984]. The enclosing volume was centered at an altitude of 10 km. The phase of each scatterer is dictated by the two-way path length from the transmitter to the scatterer and back to the receiver. For our study of RIM, the transmitter and receiver are collocated. Of course, the phase is also dependent on the transmitter frequency, which was

varied over the six values 49.5, 49.7, 49.9, 50.1, 50.3, and 50.5 MHz. An additional signal was generated at the system center frequency of 50.0 MHz. Future work will include a study of the advantages of nonredundant frequency spacing. Standard texts on array processing, which has many similarities to the current situation, have explored the advantages of nonredundant spacing [*Johnson and Dudgeon*, 1993]. Assuming adequate sampling in frequency, the main advantage will be the reduction of range aliasing. However, the range weighting function formed by the pulse inherently mitigates such problems.

As in all interferometric measurements, the phase difference between the signals should be known. As mentioned earlier, RIM is no exception in that the initial phase (ϕ_i) of the m signals should be known, or measured. An exception is if the m signals have the same initial phase, in which case all cross-spectral calculations would inherently cancel the initial phase. If this cannot be accomplished, the initial phase could be estimated by leaking the transmitted signal to the receiver and measuring the phase of each signal. Any inaccuracy in the phase measurements would have an effect of "defocusing" the estimate of range brightness. Results from an investigation of this effect will be presented at the end of this section.

Using the simulation routine with 200 randomly located scatterers, five records of 256 time series points with a sampling time of 0.1 s were generated. Initial phase was set to zero on all frequencies so that the algorithms could be easily compared. The mean horizontal wind was set to be northerly, with a magnitude of 30 m s^{-1}. Except for isotropic turbulent fluctuations, no vertical motion was used. The root-mean squared (RMS) magnitude of the turbulence was set to 0.5 m s^{-1}, with a spatial correlation scale of 10 m. After generation of the time series, additive, white Gaussian noise was introduced, producing a signal-to-noise ratio (SNR) of 20 dB.

In addition to the range weighting function of the 1-μs pulse, a simulated scattering layer was introduced with an arbitrary width of 7 m. The composite of the scattering layer and range weighting function is shown in Figure 1a. The vertical axis is height, with an extent of 150 m. Notice that the single-layer model has a Gaussian shape, as assumed by standard FDI analysis. After five incoherent integrations, resulting in an average time of approximately 2.1 min, Capon and Fourier RIM estimates of the range brightness were generated and are presented in Figure 1b as solid and dashed lines, respectively. These estimates of range brightness were obtained by scanning r_I in (7) and (8) over 100 range steps and normalizing the maximum brightness to unity. In addition, the temporal frequency (f) dependence of range brightness was eliminated through an average over all frequencies. However, advantages may exist in limiting the averaging process over a smaller band of frequencies. Such a process could be used to filter unwanted interference or to separate the range brightness from upward and downward moving parcels, for example. Notice that the result from Capon RIM more closely resembles the actual model weighting in Figure 1a. However, range resolution cannot be determined from this single-layer example. Also included in Figure 1b are the results from the 15 possible frequency combinations used with the standard FDI procedure. FDI layer position is shown by crosses, with the width being given by the error bar. From left to right, the signal combinations are $s_1(t) \leftrightarrow s_2(t)$, $s_1(t) \leftrightarrow s_3(t)$, ..., and $s_5(t) \leftrightarrow s_6(t)$. As expected, the FDI position estimates are above the actual layer height due to finite beam width effects [*Franke*, 1990]. An interesting feature is that the layer widths are overestimated in a systematic

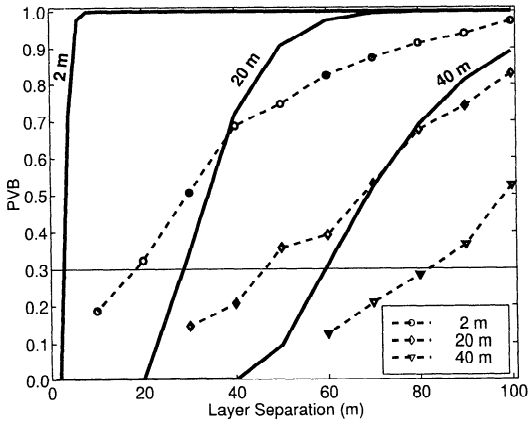

Figure 3. Peak-to-valley brightness (PVB) for Capon RIM and layer widths of 2, 20, and 40 m, as a function of layer separation. Solid lines depict PVB from the model of range brightness and therefore represent an upper bound on resolution. The corresponding dashed lines are the averaged simulation results over 50 independent realizations. A thin horizontal line at a PVB of 0.3 is provided as a reference.

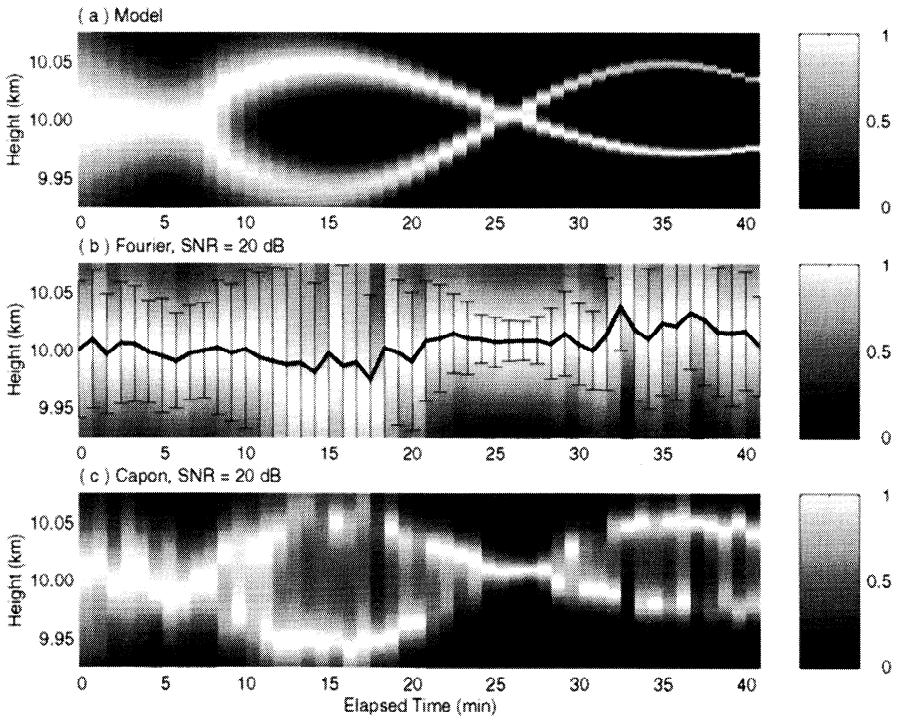

Figure 4. Simulation of two time-varying layers with position motion modeled in a sinusoidal manner. Range brightness is estimated using six frequencies and is given in linear units. The layer widths are decreased exponentially from 100 m to 4 m, and the SNR is set at 20 dB. (a) Model weighting within the resolution volume is shown over a 40-min time period. (b) Shown is Fourier RIM along with FDI results obtained by a median of the layer position/widths for the 15 frequency pairs. Note that FDI produces reasonable results only when a single layer can be seen, such as at 26 min. (c) Capon RIM is able to track the two layers including layer position and width.

manner. Namely, smaller frequency spacing produces a larger overestimation than frequencies which are spaced farther apart. This can be explained by a simple time domain analogy. As is well known, the frequency resolution of a Fourier-based spectral estimate is determined by the total length of the data set and is related to the convolution of the Fourier transform of the temporal window function. In the case of FDI analysis, the frequency spacing sets a "range window function" which limits the range resolution. By increasing the spacing between frequency pairs, this window function is narrowed, thus producing less biased estimates of layer width. Of course, system limitations are set by the intrinsic bandwidth of the receiver. Furthermore, the correlation of scatter returned by different carrier frequencies is limited by the nature of the Bragg-scale, refractive index variations within the resolution volume.

Using the same configuration as before (SNR=20 dB), we have generated a new data set with two layers of equal width (7 m) and a 50-m separation centered at 10 km. Again, the initial phase was set to zero. The model weighting is shown in Figure 2a. Two-frequency FDI analysis was first derived under the assumption of a single scattering layer [*Kudeki and Stitt*, 1987]. As a result, it is shown in Figure 2b that all frequency pairs produce similar FDI results in position and width, except for the frequency spacing dependence mentioned previously. Under the single-layer model, the FDI analysis produces position and width estimates which closely resemble the first and second moments of the model weighting. Fourier RIM shows a single broad peak near the center of the two layers. In contrast, Capon RIM is able to discern the two layers, although a limit on range resolution is beginning to become apparent. Another

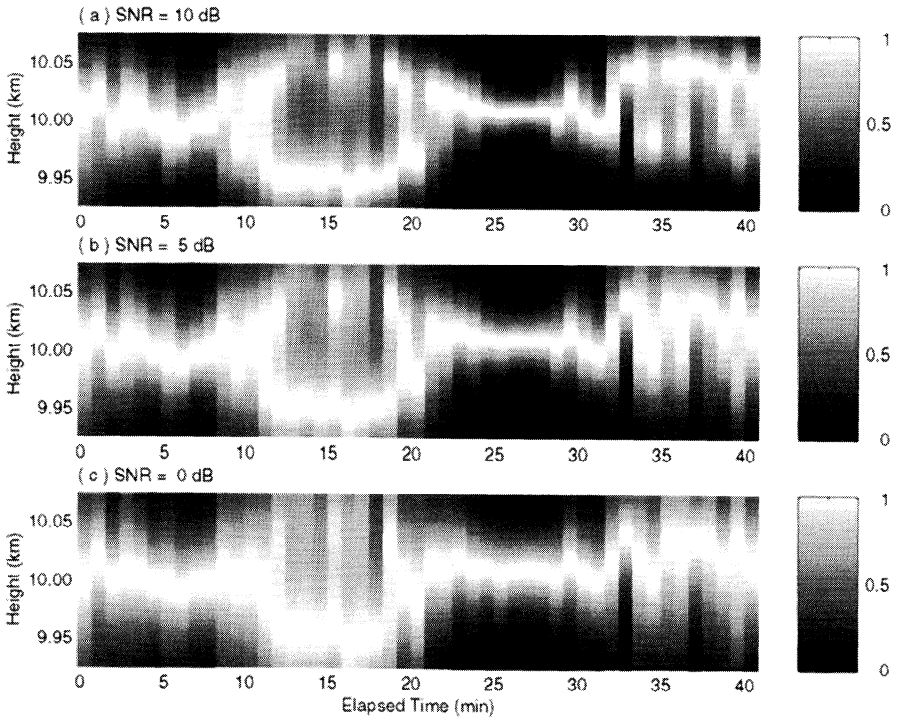

Figure 5. Same as Figure 4c for Capon RIM, except that the SNR is varied over (a) 10 dB, (b) 5 dB, and (c) 0 dB.

possible method to extend the original FDI analysis could be to derive the pertinent equations under the assumption of multiple layers. Using these equations, it might be possible to estimate position/width for each layer. However, the method would be cumbersome due to the lack of knowledge of the actual number of layers. Our development of RIM takes a completely different approach and does not require any assumptions of the number or shape of the layers.

Resolution is a difficult characteristic to quantify. Nevertheless, one "resolution measure" which can be easily calculated, for a two-layer structure, is the peak-to-valley brightness (PVB), which will be defined by the following equation:

$$\mathrm{PVB} \equiv \frac{\hat{B}_{\max} - \hat{B}_{\min}}{\hat{B}_{\max}} \tag{9}$$

The term $\hat{B}_{\max}$ is the maximum in the range brightness estimate and is usually normalized to unity. $\hat{B}_{\min}$ is the minimum of the brightness estimate, or valley, between the two peaks. The quantity PVB is bounded between 0 and 1, with higher values corresponding to superior resolution. Obviously, PVB will be dependent on the technique used and the layer width/separation. Simulated data were generated for 50 independent realizations for each combination of layer width and separation shown in Figure 3. The average PVB for Capon RIM over the 50 trials is provided in the figure as dashed lines. Two incoherent integrations were performed for these results. No noise was added to the data, providing an infinite SNR. Further, two identical layers were placed symmetrically about the center of the resolution volume. Two layers will be more easily resolved if their widths are small and are well separated. The solid lines represent PVB from the model range brightness, providing an upper bound for the simulation results. As expected, the 2-m simulation results (dashed line with circles) are always less than the 2-m model results and gradually increase with larger layer separations. This fact also holds for the 20-m and 40-m results. Generally, PVB decreases for thicker layers and smaller separation. It is also expected that the resolution measure will decrease with smaller SNR.

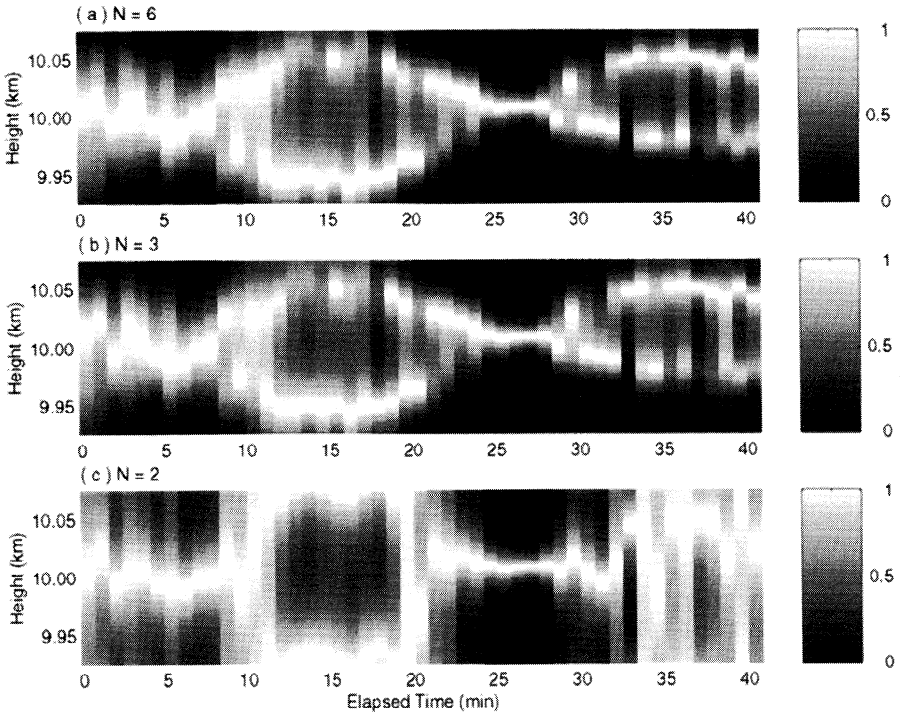

Figure 6. Same as Figure 4c for Capon RIM and SNR=20 dB, except that the number of frequencies used in the imaging procedure is varied over (a) N=6 (same as Figure 4c), (b) N=3 (49.5, 50.0, and 50.5 MHz), and (c) N=2 (49.5, and 50.5 MHz). Notice that the N=2 case shows distinct signs of undersampling, although the gross details are imaged.

However, the intent here was to quantify the best possible resolution as a function of layer width and separation only.

As an example of the use of this analysis, assume that a PVB of 0.3 is needed in order to easily resolve two peaks. For this case, Figure 3 shows that 2-m layers could be resolved using Capon RIM if they are separated by at least 20 m. Layers with widths of 40 m would need a minimum separation of approximately 80 m. Of course, a generalization of the minimum layer separation would depend on the bandwidth, among other system and atmospheric characteristics.

In order to further test the resolution capabilities of RIM in a more realistic (albeit qualitative) manner, a sequence of 100 records of 256-point data sets were generated. In this case, the positions and widths of the two layers were varied to create a structure similar to a KH billow. After incoherently averaging two records, the resulting model weighting had the form shown in Figure 4a. The layer widths were decreased exponentially over the entire duration of the data set from 100 m to 4 m. Again, the SNR was set to 20 dB. Results from Fourier RIM and a median of the FDI results from the 15 frequency pairs are shown in Figure 4b. The resolution of Fourier RIM is not adequate to distinguish the structure. In contrast, the Capon RIM results shown in Figure 4c clearly reconstruct the original model structure. The dependence of Capon RIM on SNR, where the SNR was set to 10, 5, and 0 dB, is shown in Figure 5. Notice the severe degradation in clarity and resolution. For example, the second billow pattern at an elapsed time of 35 min is not easily distinguished for even a SNR of 10 dB. However, the larger billow at 15 min is more readily observed.

The effect of frequency sampling will now be described. As was mentioned in the explanation of the simulation procedure, six frequencies were used, with an additional frequency set to 50.0 MHz. Using these data, the number of frequencies m was set to six (same as previous results), three (49.5, 50.0, and 50.5 MHz), and two (49.5 and 50.5 MHz), and the Capon RIM was implemented. Results from Capon

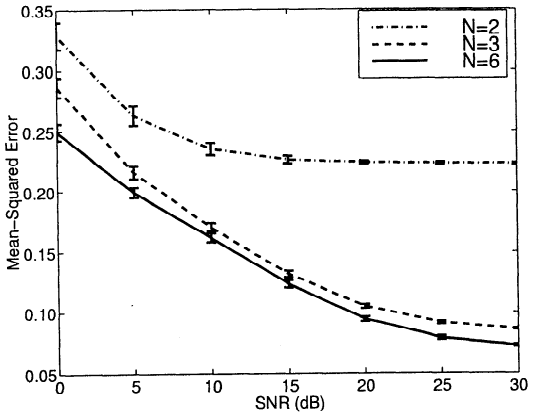

Figure 7. Mean-squared error (MSE) between the Capon RIM results and the model of Figure 4a taken on a pixel-by-pixel basis as a function of SNR. The number of frequencies was set to six, three, and two. As expected from Figure 6, the MSE is only moderately improved by increasing from three to six frequencies, for this case. However, using only two frequencies significantly degrades the results, which is an effect of undersampling. Note that the error bars are ±4 times the standard deviation.

RIM with a SNR of 20 dB are shown in Figure 6. Figure 6a is repeated from Figure 4c for comparison. Notice that by reducing from six to three frequencies, no qualitative reduction in image clarity is observed. However, using only two frequencies produces significant effects due to range aliasing. One can view RIM frequency sampling similarly to temporal sampling. Range resolution is not seriously affected by the number of frequencies since this is limited by the total frequency span and not the number of samples.

In order to quantify the results presented, we have chosen to calculate the mean-squared error (MSE) of the entire reconstructed image in comparison with the model image of Figure 4a. The MSE of Capon RIM versus SNR and for m equal to six, three, and two, is presented in Figure 7. Fifty trials of the simulation were conducted with independent noise sequences, and for each case the mean and standard deviation of the MSE were calculated. The standard deviation was extremely small compared with the mean. Therefore the error bars shown in Figure 7 are actually ±4 times the standard deviation. Expectedly, larger SNR produces lower MSE independent of the number of frequencies used. Only a small improvement in MSE is gained by increasing from three to six frequencies since the maximum frequency spread does not change for these two cases. Of course, the reader should be aware that unusually strong echoes from outside the range gate could have a detrimental effect on the range brightness estimates using only three frequencies. In this case, nonredundant frequency spacing could be used to mitigate this range aliasing effect.

Finally, the effect of error in the initial phase estimate will be investigated. Previously, the initial phase has been set to zero. In order to study phase error, we have introduced a random phase term to each time series point. The random phase is Gaussian-distributed, zero-mean, with the standard deviation varied from 0° to 30°. By increasing the standard deviation of the phase error, we expect a more significant defocusing effect and thus larger MSE. Examples of the estimated range brightness for SNR=20 dB are shown in Figure 8 for phase error standard deviation (σ_ϕ) of 5°, 15°, and 25°. Although the defocusing effect becomes more pronounced for larger σ_ϕ, the gross features of the KH billow are still evident even for σ_ϕ=15°. We anticipate that a σ_ϕ of less than 10° will produce reasonable results.

In a manner similar to Figure 7, the MSE was calculated for SNR=20 dB and 50 independent trials over the entire image. These results are shown in Figure 9 as a function of σ_ϕ for the number of frequencies equal to six, three, and two. The results show that an initial phase error with standard deviation less than approximately 10° does not cause a significant quantitative degradation in the range imaging results.

4. Conclusions

An introduction to range imaging (RIM) has been presented, which is a technique whereby frequency diversity is exploited to significantly increase the range resolution of pulsed radar systems. Frequency diversity can be achieved by transmitting m pulses with slightly different frequencies. A general framework has been presented where the m coherently detected signals could be combined using a simple weighted summation. The weight vector, or "range steering vector," is used to create constructive interference of the m signals at a particular range. By using constrained optimization (Capon's method), the estimates of "range brightness" were enhanced to a point where simulated structures similar to KH billows could be observed within the extent of the range gate. Furthermore, it was shown that the quality of

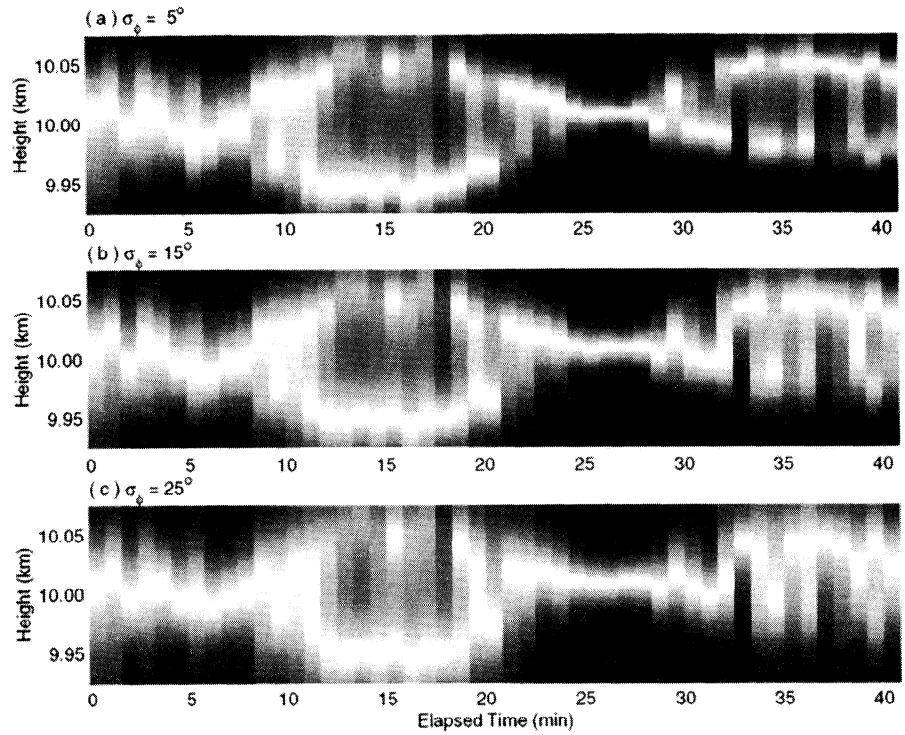

Figure 8. Same as Figure 4c for Capon RIM, SNR=20 dB, and N=6 except that a random initial phase has been introduced to the time series data. Range brightness has been estimated for a phase standard deviation (σ_ϕ) of (a) 5°, (b) 15°, and (c) 25°. As expected, larger error in the initial phase estimate emphasizes the defocusing effect.

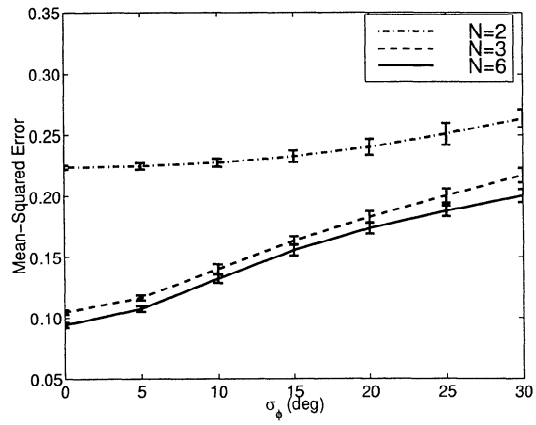

Figure 9. MSE between the Capon RIM results and the model of Figure 4a taken on a pixel-by-pixel basis as a function of initial phase error and SNR=20 dB. As in Figure 7, the number of frequencies was set to six, three, and two. A gradual increase in MSE is observed for larger phase error, although acceptable results are possible for phase error below approximately 10°. Note that the error bars are ±4 times the standard deviation.

the reconstructed images, measured by MSE, was not significantly diminished by using only three frequencies, for this case. In general, the number of frequencies should be greater than the anticipated number of significant features in the vertical structure. This does not imply that the number of features must be known a priori but only that the number of frequencies should be greater than the number of features. The effect of a smaller number of frequencies would simply be to not image the less significant features.

The flexibility achieved by using the simulation method of *Holdsworth and Reid* [1995] has also allowed the study of error in the initial phase estimates. By introducing a random phase term into each time series point, it was shown that phase error as large as 10° did not produce significant defocusing of the range brightness estimates from Capon RIM. Therefore, we believe that useful results can be obtained from Capon RIM analysis if a moderately accurate estimate of the initial phase terms is made.

With the confidence gained by these RIM simulation results, future work is currently being planned

for an experimental campaign with the sounding system (SOUSY) radar located in the Harz Mountains of Germany. A simple scheme has been devised at the SOUSY radar facility for the measurement of the initial phase terms. It is planned that the transmitted signal will be attenuated, delayed, and cycled directly back to the receiver. Measurement of this signal will then be used to estimate the initial phase terms. In addition to the SOUSY experiments, possible advantages of nonredundant frequency spacing will be investigated in future simulation research in order to design the minimum system requirements needed for the successful use of RIM for the observation of small-scale structures.

Acknowledgments. R.D.P. and T.Y.Y. were supported by the Division of Atmospheric Sciences of the National Science Foundation through grant ATM 94-02021. P.B.C. was supported by the Environment and Space Research Institute (MRI) in Kiruna. The authors would like to thank H. Ninh for his help with the initial simulations. The authors also thank G. Schmidt for his input on the measurement of initial phase and his help in the planning of the future SOUSY radar experiments.

References

Capon, J., High-resolution frequency-wavenumber spectrum analysis, *Proc. IEEE*, *57*(8), 1408–1419, 1969.

Chilson, P. B., A. Muschinski, and G. Schmidt, First observations of Kelvin-Helmholtz billows in an upper level jet using VHF frequency domain interferometry, *Radio Sci.*, *32*(3), 1149–1160, 1997.

Cho, J. Y. N., and J. Röttger, An updated review of polar mesosphere summer echoes: Observation, theory, and their relationship to noctilucent clouds and subvisible aerosols, *J. Geophys. Res.*, *102*(D2), 2001–2020, 1997.

Dalaudier, F., D. Sidi, M. Crochet, and J. Vernin, Direct evidence of "sheets" in the atmospheric temperature field, *J. Atmos. Sci.*, *51*(2), 237–248, 1994.

Doviak, R. J., and D. S. Zrnić, Reflection and scatter formula for anisotropically turbulent air, *Radio Sci.*, *19*(1), 325–336, 1984.

Eaton, F. D., S. A. McLaughlin, and J. R. Hines, A new frequency-modulated continuous wave radar for studying planetary boundary layer morphology, *Radio Sci.*, *30*(1), 75–88, 1995.

Franke, S. J., Pulse compression and frequency domain interferometry with a frequency-hopped MST radar, *Radio Sci.*, *25*(4), 565–574, 1990.

Franke, S. J., J. Röttger, C. La. Hoz, and C. H. Liu, Frequency domain interferometry of polar mesosphere summer echoes with the EISCAT VHF radar, *Radio Sci.*, *27*(3), 417–428, 1992.

Hocking, W., Radar studies of small scale structure in the upper middle atmosphere and lower ionosphere, *Adv. Space Res.*, *7*(10), 327–338, 1987.

Hocking, W. K., Recent advances in radar instrumentation and techniques for studies of the the mesosphere, stratosphere, and troposphere, *Radio Sci.*, *32*(6), 2241–2270, 1997.

Holdsworth, D. A., and I. M. Reid, A simple model of atmospheric radar backscatter: Description and application to the full correlation analysis of spaced antenna data, *Radio Sci.*, *30*(4), 1263–1280, 1995.

Hysell, D. L., Radar imaging of equatorial *F* region irregularities with maximum entropy interferometry, *Radio Sci.*, *31*(6), 1567–1578, 1996.

Johnson, D. H., and D. E. Dudgeon, *Array Signal Processing*, Prentice-Hall, Englewood Cliffs, N. J., 1993.

Kay, S., *Modern Spectral Estimation: Theory and Application*, Prentice-Hall, Englewood Cliffs, N. J., 1987.

Kudeki, E., and G. R. Stitt, Frequency domain interferometry: A high-resolution radar technique for studies of atmospheric turbulence, *Geophys. Res. Lett.*, *14*(3), 198–201, 1987.

Kudeki, E., and F. Sürücü, Radar interferometric imaging of field-aligned plasma irregularities in the equatorial electrojet, *Geophys. Res. Lett.*, *18*(1), 41–44, 1991.

Luenberger, D. G., *Linear and Nonlinear Programming*, Addison-Wesley, Reading, Mass., 1984.

Muschinski, A., and C. Wode, First in situ evidence for coexisting submeter temperature and humidity sheets in the lower free troposphere, *J. Atmos. Sci.*, *55*, 2893–2906, 1998.

Muschinski, A., P. B. Chilson, S. Kern, J. Nielinger, G. Schmidt, and T. Prenosil, First frequency-domain interferometry observations of large-scale vertical motion in the atmosphere, *J. Atmos. Sci.*, *56*, 1248–1258, 1999.

Palmer, R. D., S. Gopalam, T. Yu, and S. Fukao, Coherent radar imaging using Capon's method, *Radio Sci.*, *33*(6), 1585–1598, 1998.

Reid, I. M., Radar observations of stratified layers in the mesosphere and lower thermosphere (50-100 km), *Adv. Space Res.*, *10*(10), 7–19, 1990.

Woodman, R. F., Coherent radar imaging: Signal processing and statistical properties, *Radio Sci.*, *32*(6), 2373–2391, 1997.

P. B. Chilson, MRI Atmospheric Research Programme, Swedish Institute of Space Physics, Box 812, S-981 28 Kiruna, Sweden. (e-mail: Phillip.Chilson@irf.se)

R. D. Palmer and T.-Y. Yu, Department of Electrical Engineering, University of Nebraska, Lincoln, NE 68588-0511. (e-mail: rpalmer2@unl.edu; tian@doppler.unl.edu)

(Received February 12, 1999; revised July 26, 1999; accepted August 9, 1999.)